

# Cone-beam breast computed tomography with a displaced flat panel detector array

Giovanni Mettivier<sup>a)</sup> and Paolo Russo

*Università di Napoli Federico II, Dipartimento di Scienze Fisiche, and INFN, Sezione di Napoli, I-80126 Napoli, Italy*

Nico Lanconelli and Sergio Lo Meo

*Alma Mater Studiorum-Università di Bologna, Dipartimento di Fisica, and INFN, Sezione di Bologna, I-40127 Bologna, Italy*

(Received 18 August 2011; revised 2 April 2012; accepted for publication 3 April 2012; published 25 April 2012)

**Purpose:** In cone-beam computed tomography (CBCT), and in particular in cone-beam breast computed tomography (CBBCT), an important issue is the reduction of the image artifacts produced by photon scatter and the reduction of patient dose. In this work, the authors propose to apply the detector displacement technique (also known as asymmetric detector or “extended view” geometry) to approach this goal. Potentially, this type of geometry, and the accompanying use of a beam collimator to mask the unirradiated half-object in each projection, permits some reduction of radiation dose with respect to conventional CBBCT and a sizeable reduction of the overall amount of scatter in the object, for a fixed contrast-to-noise ratio (CNR).

**Methods:** The authors consider a scan configuration in which the projection data are acquired from an asymmetrically positioned detector that covers only one half of the scan field of view. Monte Carlo simulations and measurements, with their CBBCT laboratory scanner, were performed using PMMA phantoms of cylindrical (70-mm diameter) and hemiellipsoidal (140-mm diameter) shape simulating the average pendant breast, at 80 kVp. Image quality was evaluated in terms of contrast, noise, CNR, contrast-to-noise ratio per unit of dose (CNRD), and spatial resolution as width of line spread function for high contrast details.

**Results:** Reconstructed images with the asymmetric detector technique deviate less than 1% from reconstruction with a conventional symmetric detector (detector view) and indicate a reduction of the cupping artifact in CT slices. The maximum scatter-to-primary ratio at the center of the phantom decreases by about 50% for both small and large diameter phantoms (e.g., from 0.75 in detector view to 0.40 in extended view geometry at the central axis of the 140-mm diameter PMMA phantom). Less cupping produces an increase of the CT number accuracy and an improved image detail contrast, but the associated increase of noise observed may produce a decrease of detail CNR. By simulating the energy deposited inside the phantoms, the authors evaluated a maximum 50% reduction of the absorbed dose at the expense of a decrease of CNR, for the half beam irradiation of the object performed with the displaced detector technique with respect to full beam irradiation. The decrease in CNR, and in absorbed dose as well, translates into a detail CNRD showing values comparable to or higher than the ones obtained for a conventional symmetric detector technique, attributed to the effect of decreased scatter in particular at the axis of the irradiated object. An estimate is provided (about 12%) for the average dose reduction possible in CBBCT at constant CNR for the average uncompressed breast (14 cm diameter, 50% glandularity), in case of minimum image overlapping in extended view.

**Conclusions:** Simulations and experiments show that CBCT reconstructions with the displaced detector technique and with a half beam collimator are less affected by scatter artifacts, which could lead to some decrease of the radiation dose to the irradiated object with respect to a conventional reconstruction. This dose reduction is associated with increase of noise, decrease of CNR, but equal or improved CNRD values. The use of a small area detector would allow also to reduce the apparatus cost and to improve the data transfer speed with a corresponding increment of frame rate. © 2012 American Association of Physicists in Medicine. [<http://dx.doi.org/10.1118/1.4704641>]

Key words: cone-beam computed tomography, cone-beam breast computed tomography, dose reduction, scatter reduction

## I. INTRODUCTION

This work describes the implementation of a dedicated acquisition technique for x-ray computed tomography (CT) with cone-beam geometry, with specific application to breast CT.

### I.A. Displaced detector techniques

Cone-beam computed tomography (CBCT) imaging technique is a procedure of increasing relevance both in the medical imaging research and clinical practice. The principal feature of CBCT is the direct three-dimensional (3D) reconstruction. The “exact” 3D reconstruction can be achieved by the conventional backprojection algorithm developed by Feldkamp *et al.*,<sup>1</sup> starting from a complete 2D projection dataset acquired with cone-beam geometry over an angular range of 360°.

When an object extends outside of the scan field of view (FOV), the tomographic data are truncated. Because of non-locality of the filtered-backprojection reconstruction, such truncation results in image artifacts that propagate from the edge of truncation toward the center, distorting the whole image. When the data are truncated on only one side of the detector, the missing data can be compensated using the complementary data on the asymmetric side of the detector, acquired during the half rotation containing views of the second half of the object. Thus, in order to cover a FOV that extends outside the coverage of the physical detector, it makes sense to shift the detector such that it covers the extended FOV on one side. Circular orbit CBCT reconstruction techniques, using a weighting function to compensate the missing data in cone-beam geometry, were suggested by Cho *et al.*<sup>2</sup> They are variants of Feldkamp’s filtered backprojection algorithm, and given an appropriate amount of overscan, they provide satisfactory reconstruction. In Ref. 2, two correction methods were proposed. The first one involved the use of preconvolution weighting of the ray sums in the vicinity of any abrupt discontinuities. The weighting function transforms the edge gradient to a smooth, nonsingular profile. The second method performs a postconvolution weighting preceded by a nonzero estimation of the missing data. Each missing ray is estimated as the ray that passes through the object in the appropriate plane. These data appear in the view acquired when the source is approximately on the opposite side of the object.

The weighting function approach was repropounded by Wang for circular orbit micro-CT (Ref. 3) and then generalized for helical reconstruction.<sup>4</sup> A further generalization of these methods was proposed by Zamyatin *et al.*,<sup>5</sup> which enables the use of different algorithms, such as short-scan.

### I.B. Cone-beam breast computed tomography

In the last decade, with the development of flat panel detectors, the CBCT imaging technique has made significant progress in CT systems integration and in applications where the cone-beam geometry provides fast 3D imaging. In particular, cone-beam breast CT (CBBCT), with flat panel detectors dedicated to image the female breast, represents a

promising modality for the diagnosis of breast cancer,<sup>6–8</sup> whose interest has been renewed by Boone *et al.*<sup>6</sup> in 2001 after initial studies in the 1970s with older CT technology. A number of dedicated scanners have been developed by several authors<sup>9–13</sup> as well as by our group.<sup>14,15</sup> CBBCT provides 3D volumetric image reconstruction from 2D projections acquired in orbit around the patient. This allows to overcome the problem of overlapped tissue structures provided by conventional two views (craniocaudal and mediolateral oblique) x-ray mammography of the compressed breast.

However, the use of this 3D breast imaging technique poses some questions:

- For use in screening studies, the related mean glandular dose (MGD) should not exceed the corresponding limit for two-view mammography, i.e.,  $2 \times 2.5$  mGy for a standard breast, according to the European standard<sup>16,17</sup> (or  $2 \times 3.0$  mGy, in the USA standard<sup>6,18</sup>). However, no such stringent dose requirements are necessary for clinical (no screening) examinations.
- The presence of a great photon scatter fraction in the projection images.<sup>19–21</sup> This fraction is usually much larger than the one occurring in x-ray mammography with a compressed breast and a low-energy x-ray beam, and it is significant also with respect to fan-beam CT, where the cone angle is about ten times lower. The presence of scatter reduces contrast and also contributes additional x-ray quantum noise and attenuation underestimation at the center of the object (cupping artifact). Scattering within the breast also contributes additional dose to the breast, which does not necessarily contribute to corresponding improvements in image quality. It is possible to fix these types of artifacts using software scatter correction methods.<sup>22–27</sup> These methods reduce the effects of scatter in the reconstructed volumes; it would be beneficial to use scatter rejection techniques, which could also reduce the dose to the patient. Recently, it has been suggested<sup>13,28</sup> that in order to improve microcalcification visibility, a micro-CBBCT setup should offer a spatial resolution in the order of 0.1 mm, by adopting fine-focus x-ray tubes and fine pitch detectors.
- The requirement to operate with a magnification factor between 1.5 and 2.2 to reduce scatter influence via a suitable air gap<sup>19</sup> and to optimize the system modulation transfer function,<sup>29</sup> coupled with the necessity to have a FOV ranging from 12 to 36 cm to image uncompressed breasts with a diameter ranging from 5 to 18 cm as found by Huang *et al.*<sup>30</sup>

### I.C. Displaced detector techniques in CBBCT

With the aim of reducing some of the above limitations, in this paper, we apply the detector displacement technique to CBBCT. This well-tested geometry, coupled with high resolution flat panel detectors, could allow to realize a variable-FOV scanner employing a small area detector with a fine pitch: this setup allows a wider range of breast sizes to be imaged without truncation in the reconstructions. This is the obvious motivation for the application of displaced

detector geometries (i.e., “see more with a small detector”); however, it is the authors’ opinion that another important result of this technique received relatively little attention in the literature. Indeed, with the displaced detector technique, there is the possibility to irradiate only part of the phantom in each view: this is expected to provide a lower radiation dose to the scanned object (e.g., breast) in addition to a lower scatter fraction.

The half-beam irradiation can be achieved with a suitable beam-collimator that masks half of the object volume, when a half-FOV detector is used. Indeed, following the above considerations, if the peculiar advantages of the displayed detector geometry are demonstrated and, at the same time, the possible decrease of the image quality associated with a lower radiation dose are ascertained, then its implementation would be beneficial in terms of dose reduction and scatter reduction even in dedicated CBBCT scanners, which employ a large-area detector (e.g.,  $30 \times 40 \text{ cm}^2$  sensitive area). In this case, the detector is not displaced, but a half-beam is employed, which irradiates the half breast in a circular full orbit. Finally, the use of a smaller detector allows also to reduce the overall cost of the CT scanner. It is worth noting that any potential dose reduction should always be considered together with an estimation of the associated loss in image quality. However, it is not evident both at first instance and from the analysis of the related literature, what will be the penalty in terms of reduced image quality resulting from such an imaging technique performed at a reduced dose.

In this study, we perform Monte Carlo (MC) simulations and CT acquisitions using acrylic phantoms to evaluate the proposed technique and to investigate the anticipated effects on image quality and absorbed dose, with our CBBCT laboratory prototype.<sup>15</sup> One of the main objectives of this paper is to achieve an experimental quantification of the changes that should be expected when such technique is considered, in terms of dose, image quality, and scatter-to-primary ratio. The reported outcomes could be considered for choosing the best tradeoff between dose and image quality.

## II. MATERIALS AND METHODS

### II.A. Experimental setup

In order to evaluate the proposed method, we used both MC simulations and CT acquisitions. For the CT scans, we employed the bench-top prototype CT/SPECT scanner developed at Federico II University in Napoli<sup>15</sup> (Fig. 1) consisting of (for the CT part):

- Computer-controlled minifocus x-ray tube (SB-80-250, Source-Ray Inc., Bohemia, NY), operated at 80 kVp with a tube current of 0.25 mA. The tube has a fixed tungsten anode, a carbon fiber window, a  $50 \mu\text{m}$  minimum focal spot size, and an inherent filtration of 1.8 mm Al. Additional filtration of the beam is provided by a 0.2 mm Cu filter. At 80 kVp, the measured half value layer was 5.6 mm Al. A four-blades W collimator in front of the x-ray source allows to produce a truly cone-beam, a half cone-beam, or a fan

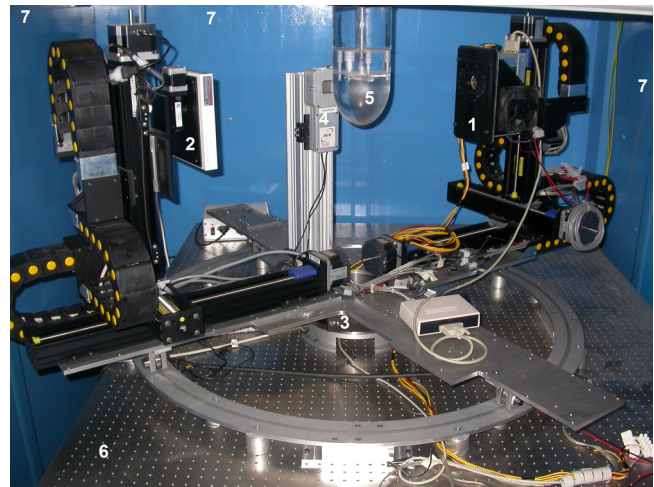


Fig. 1. Photograph of the prototype developed at University of Naples “Federico II” for cone-beam breast CT/SPECT for laboratory investigations. (1) X-ray tube, (2) flat panel detector, (3) rotating gantry, (4) pinhole compact gamma camera, and (5) PMMA breast phantom. The scanner is mounted on an optical bench (6) ( $1.5 \times 1.8 \text{ m}^2$ ) and housed in a shielded (3 mm Pb) cabinet (7).

beam. The air kerma at isocenter (385 mm from the focal spot) was 2.5 mGy for a circular orbit around the phantoms during a CT scan; this value was measured with a calibrated ionization chamber (mod. 20X6-6, with mod. 2026C dose-meter, Radcal Corp., Monrovia, CA);

- CMOS Flat Panel sensor mod. C7942CA-02 (Hamamatsu Photonics K. K., Hamamatsu City, Japan), a high resolution CsI:Tl scintillator sensor, composed of  $2240 \times 2344$  square active pixels of  $50\text{-}\mu\text{m}$  pitch ( $11.20 \times 11.72 \text{ cm}^2$  sensitive area), with a 0.15-mm thick scintillator layer. It can be operated in  $1 \times 1$ ,  $2 \times 2$ , or  $4 \times 4$  binning mode. It is read out by a digital frame grabber board via RS-422 interface (IMAQ PCI-1424 from National Instruments, Austin, TX).
- Two couples of rotating arms positioned along the longitudinal and horizontal axis of the scanner, respectively. One arm holds the x-ray tube, and the opposite arm holds the flat panel detector. The scanner comprises eight computer-controlled step motors (Velmex Inc., Bloomfield, NY). A step-motor rotation stage (mod. RV240PP, Newport Co., Irvine, CA) controls the gantry rotation. Three axis motorized linear stages are present in these two arms, and another rotator is placed behind the flat panel detector, for aligning its row-columns axes with the axes of the scanner. The scanner operates either in continuous or in step-and-shoot mode.

### II.B. Simulations

To model via MC simulations the CT scans made with this CBBCT apparatus, we used the GEANT4 code system (version 4.9.0, with the standard transport model and library of electromagnetic interactions, EM Standard library). The standard EM package provides simulation of ionization, bremsstrahlung, and other electromagnetic interactions of particles with matter.<sup>31–33</sup>

For the W anode x-ray tube [80 kVp, 1% ripple], a spectrum calculated with Boone’s TASMIP code<sup>34</sup> was used. We

tallied the photons impinging on the detector area, separating results for primary photons and photons having undergone any scattering event within the phantom. For each pixel, the scatter (S) to primary (P) ratio ( $SPR = S/P$ ) was estimated as the ratio between the energy deposited by scattered and primary photons.

For the evaluation of the proposed technique, we used two PMMA phantoms: a small cylindrical phantom (phantom 1) and a large hemiellipsoidal phantom (phantom 2). The first phantom was used for a basic validation, using MC simulations and measurements of a real complete symmetric and asymmetric dataset of the same phantom, with our scanner. The second PMMA object is a more realistic breast phantom whose diameter corresponds to the average breast size at chest wall.<sup>35</sup>

### II.C. CT reconstruction

The projections (simulated and measured) were processed using the CT cone-beam reconstruction commercial software COBRA (Exxim Computing Corporation, Pleasanton, CA) implementing the FDK algorithm. This software implements, also, a reconstruction algorithm with displaced detector on the projections:<sup>36</sup> this option was activated in the extended view reconstruction. No beam hardening correction was applied.

According to the product developer,<sup>37</sup> with reference to,<sup>38</sup> “the technique for half-beam is an extension to 3D taken from Parker’s scheme for 2D CT. Parker weighting is the common term for handling redundant rays; for example, in the center, all rays are measured twice in a 360 degree scan. In the periphery, only once. So the central rays get weight of one half.” Details in the implementation necessary to counteract inconsistencies in the data from scatter, etc., are proprietary and were not disclosed by the manufacturer.

### II.D. Phantom 1

For the MC simulation, we used a phantom designed as a uniform PMMA cylinder with a diameter of 70 mm and 100 mm height. Simulations were performed in (a) half cone-beam irradiation geometry (detector view), where the central ray of the cone-beam intersects the detector as indicated in Fig. 2(a), and (b) in extended view geometry, where the detector is displaced 50 mm laterally with respect to its position in detector view [Fig. 2(b)]. These geometries allow to acquire a complete symmetric and asymmetric dataset, respectively. Simulations were performed at an x-ray tube voltage of 80 kVp and added filtration of 0.2 mm Cu, at the fixed exposure level of 0.1  $\mu\text{Gy}$  total air kerma at isocenter for 360 views [corresponding to a photon fluence to the isocenter of about  $5 \times 10^3$  photons/ $\text{mm}^2$  over  $240 \times 240 \text{ mm}^2$ , at 80 kVp and 5.6 mm Al HVL]. This low exposure in the simulations allowed to keep short the computation time, yet at an acceptable statistics: the total number of photon histories launched was  $2.88 \times 10^8$  per simulated CT scan. The total deposited energy (MeV) at the entrance of the detector was scored in  $1 \times 1 \text{ mm}^2$  equivalent pixels over a projection area of  $240 \times 240 \text{ mm}^2$  at the detector entrance. We also scored the total energy deposited inside the phantom volume

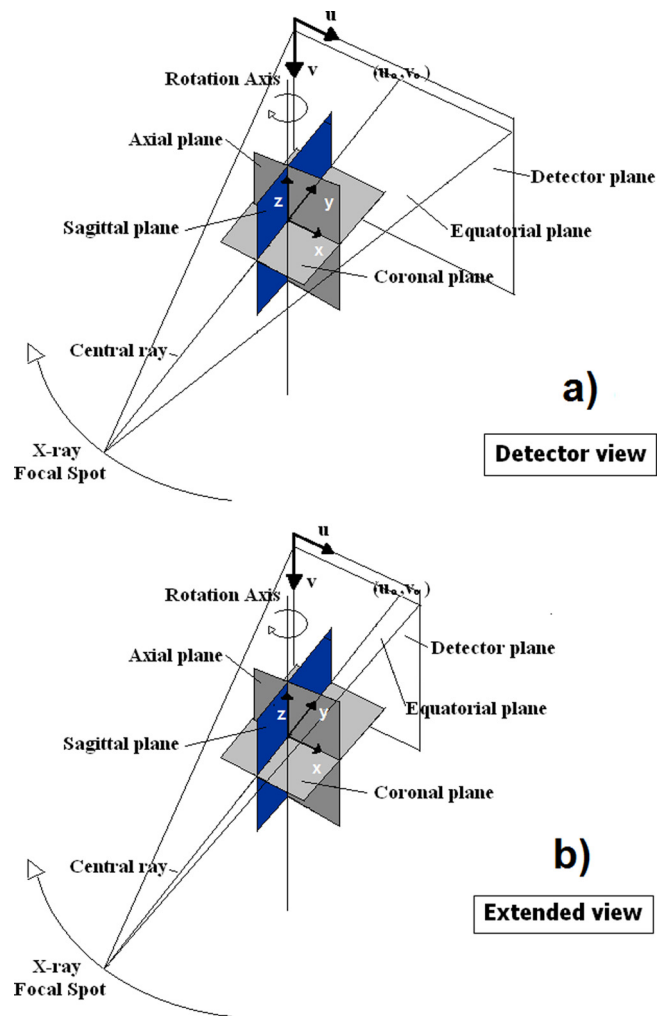


Fig. 2. Defining the “detector view” (a) and “extended view” (b) geometry.

in a cross mesh of cubic volume elements of  $10 \times 10 \times 10 \text{ mm}^3$ , from which we determined the corresponding local absorbed dose and, then, the map of the spatial distribution of absorbed dose at internal 10-mm-thick slices in the phantom, e.g., at midplane. This internal grid of voxel covers a central fraction of 49% of the cylindrical phantom volume.

For the measurements, we used a 70-mm diameter PMMA cylindrical phantom (phantom 1) composed of two inserts; each insert has a set of cylindrical holes (height = 10 mm), with varying bore size from  $\phi = 8 \text{ mm}$  to  $\phi = 0.2 \text{ mm}$  (Fig. 3). The hole axis is parallel to the rotation axis. In order to simulate fine details with varying contrast, in insert B, we put: animal fat with inclusion of three little pieces of egg shell of sizes 2.2, 1.1, and 0.5 mm (simulated calcifications) inside the 8-mm hole; four thin nylon wires ( $\phi = 0.6 \text{ mm}$ , density 1.11  $\text{g/cm}^3$ ) inside the 2-mm hole;  $\text{CaCO}_3$  calcium carbonate grains (density 2.93  $\text{g/cm}^3$ ) inside the 1-mm hole; the last 4-mm hole was air-filled. In insert A, we put extra virgin olive oil (density 0.89  $\text{g/cm}^3$ ) inside the 8-mm hole and  $\text{CaCO}_3$  calcium carbonate grains inside the 4-mm hole: the three remaining holes were air-filled. This phantom contains also two air-filled holes of  $\phi = 5 \text{ mm}$  used for insert alignment, which run axially through most of the phantom height (Fig. 3).

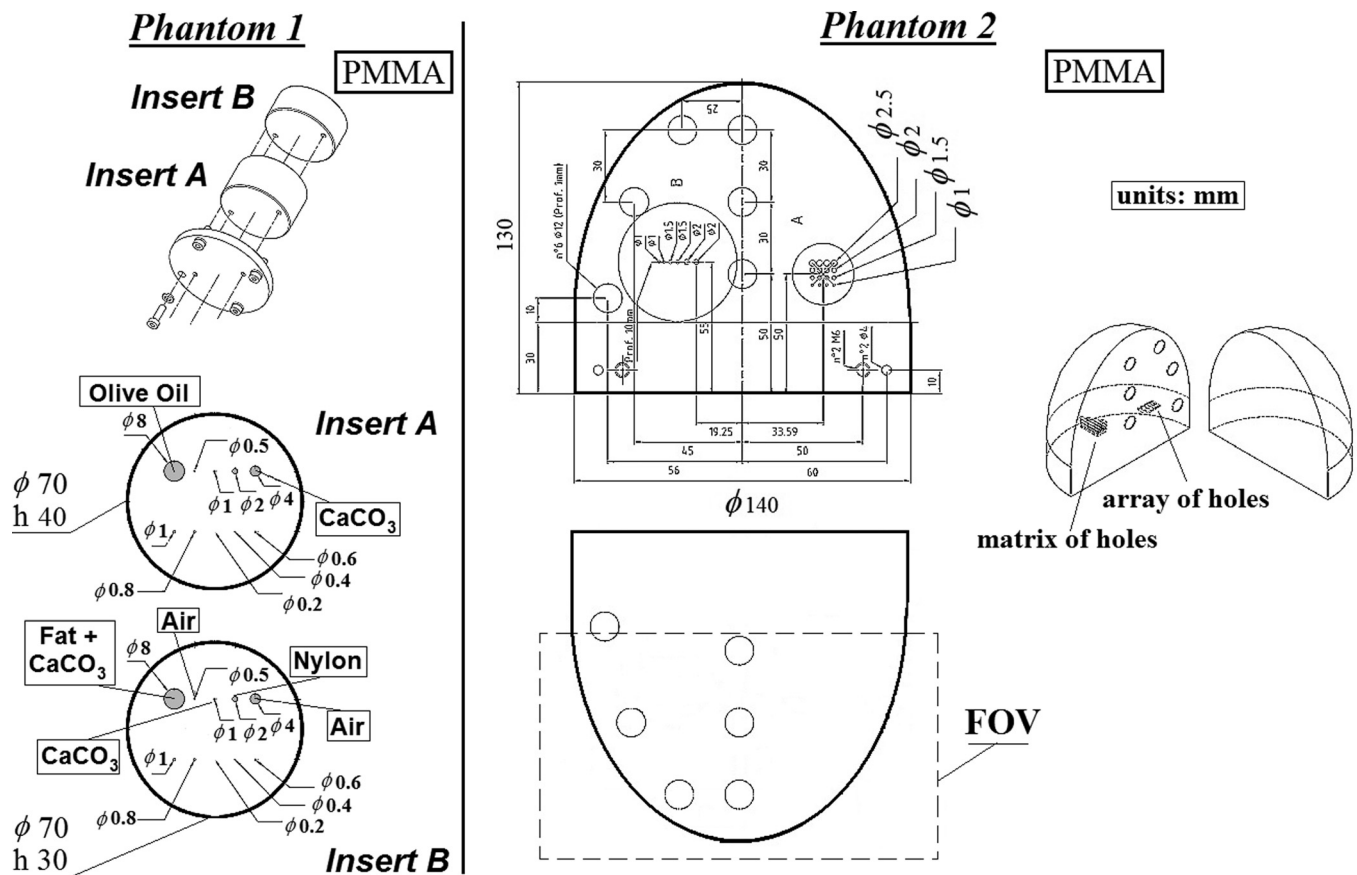


FIG. 3. Drawings of the phantoms used. Phantom 1 is a 70-mm diameter PMMA cylindrical phantom composed of two inserts. Each insert has a set of holes from  $\phi = 8$  mm to  $\phi = 0.2$  mm directed parallel to the rotation axis; phantom 2 is a PMMA volume simulating a pendant breast of 140 mm diameter at the chest wall. It consists of two half-parts held together in the geometrical form of a hemiellipsoid of rotation on a cylindrical base. The 35-mm thick cylindrical base simulates the chest wall. In one half-part are realized, at phantom midplane, six cylindrical cavities (diameter = 12 mm, depth = 1 mm). Also shown in the bottom half at right is the indication of the projection FOV during CT scan of phantom 2 (see Fig. 18).

Two types of CT scans were performed with our laboratory setup: one in detector view geometry and one with the detector displaced 50 mm laterally (extended view). In the extended view configuration, the beam was collimated in such a way as to irradiate only part ( $\cong 60\%$ ) of the phantom volume as seen by the detector, by using a lead shield placed between the source and the phantom just before it.

Both in MC simulation and CT acquisition, the phantom was positioned at the center of rotation of the scanner, at 385 mm from the x-ray source and at 120 mm from the detector (source-to-image distance = 505 mm). System magnification was 1.27 at isocenter.

The projections of phantom 1 were acquired at  $4 \times 4$  pixel binning ( $560 \times 586$  pixels) for a full scan angle of  $360^\circ$  with a step  $1^\circ$ , for a total of 360 projections, in a “step-and-shoot” modality. For image normalization, each projection was corrected for offset and gain variations by the corresponding flat-field and dark-field images, acquired in the same temporal sequence and with the same acquisition parameters as the raw data images. The CT reconstructions of the phantom 1 scans were made with a Ram-Lak filter and an isotropic voxel dimension of  $0.15 \times 0.15 \times 0.15$  mm<sup>3</sup>; the final 3D CT matrix size was  $576 \times 576 \times 640$  voxels. The axial slices and coronal/sagittal slices correspond to imaging planes orthogonal and parallel to the rotation axis, respectively ( $y$  axis in Fig. 2).

## II.E. Phantom 2

At variance with phantom 1—which was small enough to be contained in a single detector frame—phantom 2 is a realistic PMMA phantom simulating the uncompressed average breast, which cannot be contained in a single detector FOV. This homogeneous PMMA phantom has the form of a hemiellipsoid laid on a cylindrical base of 140-mm diameter; the two half-axes of the ellipsoid are 70 and 95 mm, respectively. This phantom simulates an uncompressed breast of 140-mm diameter at the chest wall, this being the average diameter of the uncompressed breast reported by Boone *et al.*<sup>35</sup> corresponding to a compressed breast thickness of about 50 mm. Also, in this case, the projections of the phantom were simulated (via GEANT4 MC code) in the two geometries, detector view and extended view, in the same conditions as for phantom 1. In this case, the internal cross mesh realized to score the total energy deposited inside the phantom volume, the corresponding local absorbed dose, and the map of the spatial distribution of absorbed dose at midplane covers a fraction of 71% of the phantom volume.

CT scans were acquired for a real phantom as the one simulated above. This phantom 2 (Fig. 3), designed in-house, consists of two half-parts machined from two blocks of PMMA (1.19 g/cm<sup>3</sup>) held together in the geometrical form of

a hemiellipsoid of rotation on a cylindrical base of 140-mm diameter. The hemiellipsoid has half-axes, of 70 and 95 mm, respectively. In one half-part, we realized, at phantom mid-plane, six air-filled cylindrical cavities (diameter = 12 mm, depth = 1 mm). In the same half-part, we realized two sets of resolution details in the form of cylindrical holes with axis perpendicular to system rotation axis. The phantom was positioned with its axis of symmetry along the axis of rotation of the scanner ( $z$  axis) at 385 mm from the x-ray source and 100 mm from the detector. In this case, system magnification was 1.26 at isocenter.

Also, in this case, two scans were performed: one in detector view and one in extended view. In detector view, due to the size of phantom 2 exceeding the detector FOV, in order to collect the complete symmetric data, we need to perform two successive scans by shifting laterally the position of the flat panel detector by a distance of a few centimeters, allowing for some image overlap between the two adjacent images (Fig. 4). This resulted in a total of 420 combined projections of  $1000 \times 586$  pixels ( $0.2 \text{ mm} \times 0.2 \text{ mm}$  pixel size after  $4 \times 4$  binning), equally sampled over  $360^\circ$ , acquired in a continuous mode acquisition of 60 s scan time at a frame rate of 7 fps. The combined FOV ( $200.0 \times 117.2 \text{ mm}^2$ ) covered an axial extent as shown by the dashed rectangle in Fig. 3. Due to the very fine detector pitch, an empirical procedure was used in order to determine the correct lateral offset in the combined projections. The correct offset was found via an image difference method explained in a previous work<sup>28</sup> based on a trial and error procedure.

In extended view, the projections were acquired at  $4 \times 4$  pixel binning ( $560 \times 586$  pixels, pixel size =  $0.2 \text{ mm} \times 0.2 \text{ mm}$ ), for a total of 420 projections over a full scan angle of  $360^\circ$ , in continuous mode. It is worth noting that, at variance with case of phantom 1, in this setup, no beam collimation was adopted: in other terms, the full beam irradiates the whole phantom so that the absorbed dose is the same in

extended and in the detector view, and any difference in the image quality in the CT scans can thus be attributed only to the reconstruction method.

The CT reconstructions of phantom 2 were made with a Ram-Lak filter and an isotropic voxel dimension of  $0.3 \times 0.3 \times 0.3 \text{ mm}^3$ ; the final 3D CT matrix size was  $512 \times 512 \times 320$  voxels.

## II.F. Image quality analysis

In order to quantify the effect of the acquisition geometry on the image quality, we evaluated different figures of merit such as:

- the (percent) image nonuniformity, NU, defined in relation to the magnitude of the cupping artifact:

$$NU \equiv \frac{CT_p - CT_c}{CT_p + 1000} \times 100\%,$$

where  $CT_c$  and  $CT_p$  [in Hounsfield units (HU)] refer to the mean CT-number in a circular ROI of a reconstructed slice near the center or the periphery of the phantom in a coronal slice, respectively;

- the image noise, as  $\text{Noise} \equiv \sigma$ , where  $\sigma$  is the standard deviation of the CT number values (HU) in an ROI at the centre of the CT slice image;
- the contrast,  $\Delta HU \equiv |\mu_D - \mu_B|$  (in HU), in the CT image for each detail (i.e., the contrast between the detail and PMMA phantom material), calculated as the absolute difference between the mean CT number values measured in an ROI of the same diameter in the detail ( $\mu_D$ ) and in the background ( $\mu_B$ );
- the contrast to noise ratio (CNR) as:

$$\text{CNR} \equiv \frac{|\mu_D - \mu_B|}{\sigma_B},$$

where  $\sigma_B$  and  $\mu_B$  are, respectively, the standard deviation and the mean value of the CT number values in an ROI in the background and  $\mu_D$  is the mean value in an ROI of the same diameter in the detail; the background was evaluated in a homogeneous coronal slice adjacent to the selected coronal slice containing the detail, at the same position as the detail.

- the contrast-to-noise ratio per unit dose (CNRD,  $\text{Gy}^{-1/2}$ ), calculated as the ratio of CNR to the square root of the absorbed dose:

$$\text{CNRD} \equiv \frac{\text{CNR}}{\sqrt{\text{Dose}}},$$

where the CNR is evaluated (experimentally) as previously indicated on measured CT slices and dose is estimated from MC simulation as the average absorbed dose (in units of  $10^{-8} \text{ Gy}$ ) obtained by dividing the total energy deposited in the internal volume mesh by the total mass of this sample volume inside the phantom;

- the CT reconstruction accuracy throughout the whole FOV in the CT image, using the relative root-mean-square (rms) error expressed in percent, as defined in Ref. 5, between the pixel values  $I_{i,j}$  (in HU units) in the image reconstructed in

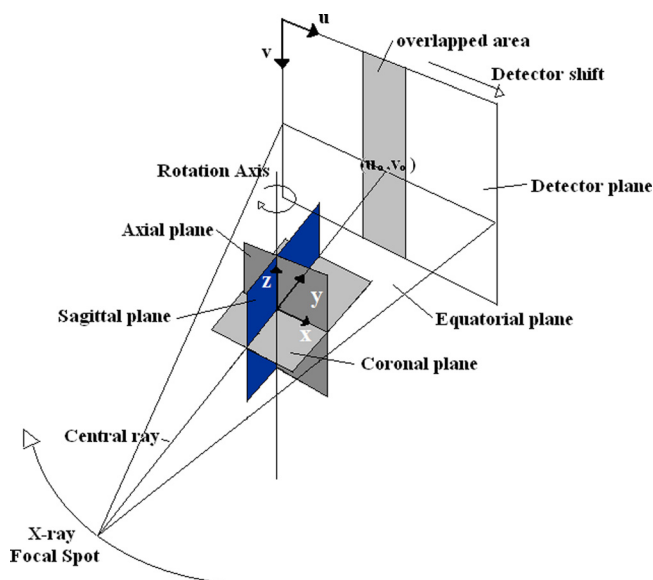


Fig. 4. Geometry utilized in “detector view” modality for the scanning of phantom 2.

extended view ( $I^E$ ) and in the image reconstructed in detector view ( $I^D$ ):

$$\text{rms\_error}(\%) \equiv \frac{\sqrt{\frac{1}{M} \sum_{i,j=1}^N (I_{i,j}^E - I_{i,j}^D)^2}}{\sqrt{\frac{1}{M} \sum_{i,j=1}^N (I_{i,j}^D)^2}},$$

where  $M = N \times N$  is the number of reconstructed pixels inside the image;  $N = 576$  for phantom 1 or  $N = 512$  for phantom 2.

### III. RESULTS

#### III.A. Phantom 1

MC simulations of phantom 1 produced images of energy deposited at the detector surface by primary photons and by scattered photons and the corresponding distribution of SPR. Three images were derived: the first one containing only primary photons in the detector view geometry; the second one containing primary photons and scattered photons in detector view; the last one containing primary photons and scattered photons in extended view. Figure 5 shows horizontal line profiles (i.e., perpendicular to the  $z$  axis in Fig. 2) along the simulated projections of phantom 1 relative to the above three images. We observe that, in extended view geometry, the line profile (up to half the phantom diameter) is closer to the profile of the primary photon distribution than the one obtained in detector view; this is attributed to a lower scatter contribution in extended view than in detector view geometry.

Images, in both geometries, of scatter-to-primary ratio (SPR) and scatter components distributions, and corresponding horizontal profiles for phantom 1 are reported in Figs. 6 and 7, respectively, as evaluated over the rectangular ROIs indicated in Fig. 6. The SPR was estimated pixel-by-pixel as the ratio between the energy deposited by scattered and primary photons. The scatter pattern extends across the whole FOV (120 mm by side) [Fig. 7(a)] and its signal strength is about twice as greater for detector view than for extended

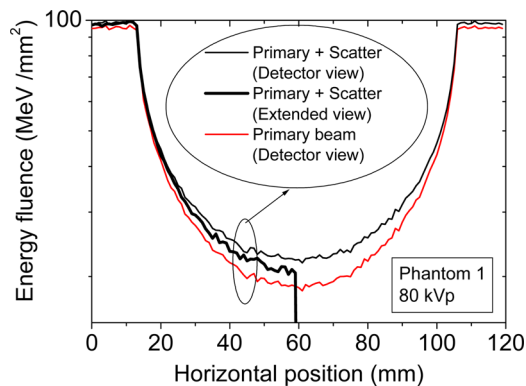


Fig. 5. Horizontal line profiles along the simulated total (primary + scatter) and primary projection images in detector view geometry and the simulated total projection in the extended view geometry for phantom 1 (70-mm diameter PMMA cylinder). A break has been inserted in the vertical scale to improve visibility of the curve differences at the center of the phantom.

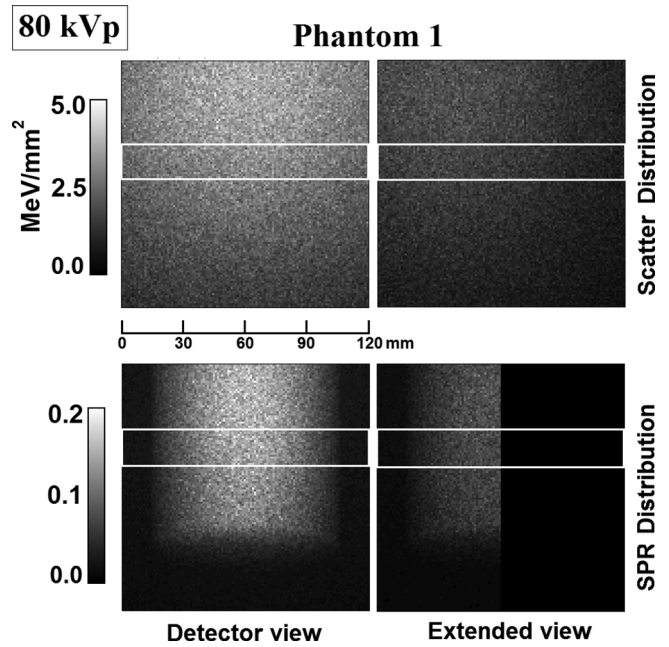


Fig. 6. Images of the simulated scatter distribution (top row) and SPR distribution (bottom row) for phantom 1 in detector view (left column) and extended view (right column). Rectangular ROIs indicated on each image were used for line profile evaluation.

view geometry. The SPR profile [Fig. 7(b)] evaluated from Fig. 6 in the indicated rectangular ROI has a Gaussian shape (or a half Gaussian shape) and its value at the center of the phantom is about 0.19 for detector view and about 0.10 for extended view, corresponding to a 53% decrease.

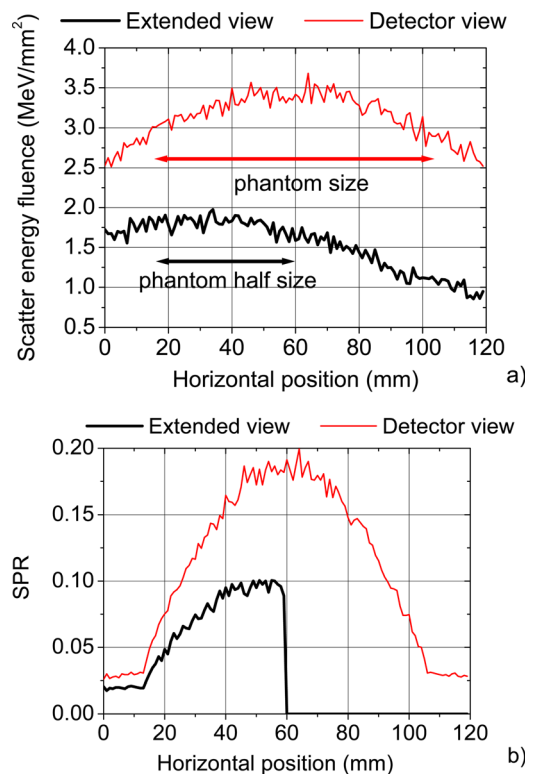


Fig. 7. (a) Scatter and (b) SPR horizontal profiles obtained from the ROIs indicated on the simulated images in Fig. 6 for phantom 1.

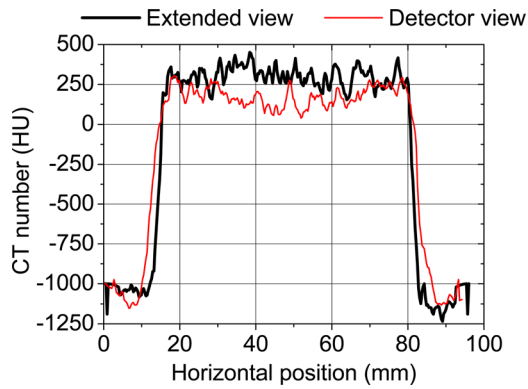


FIG. 8. Horizontal profile along the diameter of reconstructed coronal slice of phantom 1 simulated in detector and in extended views.

Figure 8 shows line profiles evaluated along the diameter of a reconstructed coronal slice of simulated phantom 1 in detector and extended view geometry, determined from MC simulations. When the extended view is adopted, the decrease of the influence of scatter in the projections produces little less cupping artifact in the CT slices than in the detector view, as indicated by a flatter profile in Fig. 8 (NU=5% for extended view and NU=6% for detector view, Table I). As regard the image noise in the simulation of phantom 1, the adoption of the extended view geometry results in an increment of noise in the reconstructed slices, by a factor 1.4 (from 136 HU to 189 HU, Table I). The reconstruction error in terms of rms\_error (%) is as little as 0.72% (Table I), indicating the good agreement between the two reconstruction methods.

TABLE I. CT global image quality parameters evaluated in coronal slices for the various phantoms and the two imaging geometries (for the definition of quantities, see Sec. II.F).

Test object	View	NU (%)	Noise (HU)	rms error (%)
Simulated phantom 1	Extended	5	189	0.72
Simulated phantom 1	Detector	6	136	
Phantom 1	Extended	14	62	0.76
Phantom 1	Detector	24	32	
Phantom 2	Extended	18	83	0.14
Phantom 2	Detector	19	78	

From the value of the energy deposited in  $10 \times 10 \times 10 \text{ mm}^3$  voxels in a mesh inside the PMMA phantom (as derived from MC simulations) we determined the local distribution of the average absorbed dose (as energy deposited in joules divided by 1.19 g mass of the voxel). Figure 9(a) shows the horizontal profile of the simulated dose distribution along a diameter in phantom 1, evaluated in correspondence of the same CT slice selected for Fig. 8. The plot in Fig. 9(a) allows to compare the dose distribution determined by the two geometries. In the case of extended view, the dose has the same trend (i.e., decreasing at the center of the phantom), but its value is almost half the corresponding value, than for detector view. The dose reduction factor [Fig. 9(b)] is between 0.49 and 0.50 throughout the profile. The 2D distribution of dose for extended view and for detector view, evaluated in a sample 10-mm-thick coronal slice at the center of the phantom 1 and shown in Fig. 9(c), is an indication that the reduction (by a factor  $\sim 2$ ) of the dose in extended view occurs

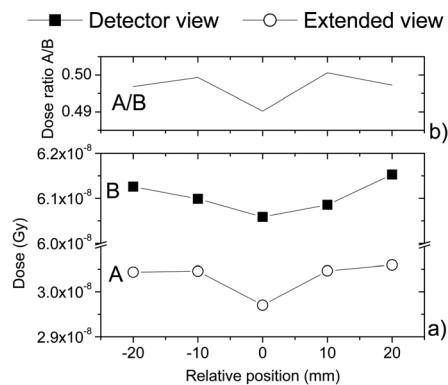


FIG. 9. Distribution of absorbed dose in phantom 1 in detector and extended view geometry, estimated in a central coronal slice from MC simulation of a CT scan with  $0.1 \mu\text{Gy}$  total air kerma at isocenter, at 80 kVp. (a) Horizontal profiles of absorbed dose along the diameter; (b) ratio between the dose in extended view and in detector view, plotted at each horizontal position in the profile; (c) map of the distribution of dose: numerical values reported (in units of  $10^{-8} \text{ Gy}$ ) represent simulated average doses in  $10 \times 10 \times 10 \text{ mm}^3$  volume elements inside the phantom 1.

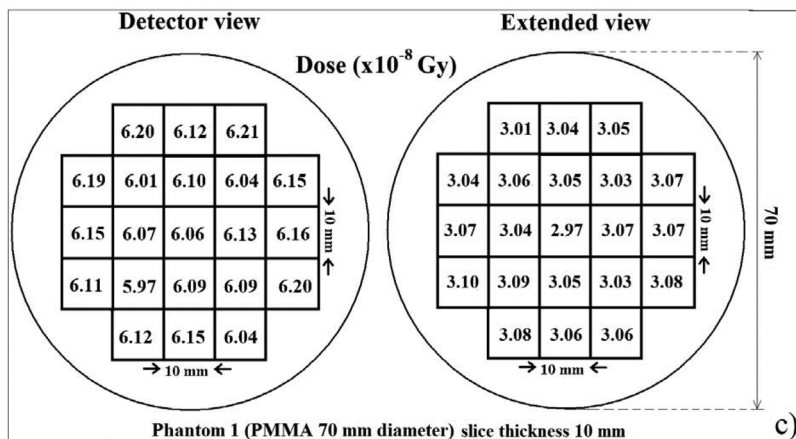


TABLE II. Detail contrast, CNR, CNRD evaluated on CT coronal slices for phantoms 1 and 2 in the extended view geometry and in detector view geometry. For CNRD, two values were calculated, from dose estimates corresponding to an object coverage of 50% and 55%, respectively.

Phantom insert	Material	Detail size (mm)	View	Contrast, $\Delta HU$ (HU)	CNR	CNRD <sup>a</sup> ( $\times 10^4$ Gy <sup>-1/2</sup> )	CNRD <sup>b</sup> ( $\times 10^4$ Gy <sup>-1/2</sup> )
Phantom 1							
B	CaCO <sub>3</sub>	1	Extended	424	14	8.3	8.1
B	CaCO <sub>3</sub>	1	Detector	314	20	8.1	8.1
B	Nylon + air	2	Extended	264	10	5.9	5.8
B	Nylon + air	2	Detector	204	8	3.2	3.2
A	Air	2	Extended	451	14	8.2	8.0
A	Air	2	Detector	339	19	8.2	8.2
B	Air	4	Extended	764	16	9.5	9.3
B	Air	4	Detector	620	14	5.7	5.7
A	CaCO <sub>3</sub>	4	Extended	1141	26	15	15
A	CaCO <sub>3</sub>	4	Detector	982	26	11	11
B	Animal fat	8	Extended	157	2.4	1.4	1.4
B	Animal fat	8	Detector	137	3.5	1.4	1.4
A	Olive oil	8	Extended	143	2.7	1.6	1.6
A	Olive oil	8	Detector	123	3.7	1.6	1.6
Phantom 2							
–	Air	2	Extended	453	14	6.0	6.0
–	Air	2	Detector	442	17	7.5	7.5

<sup>a</sup>Calculated for a dose reduction factor allowing for 50% object coverage.

<sup>b</sup>Calculated for a dose reduction factor allowing for 55% object coverage.

in most of the phantom volume and not just in a line, possibly as a result of a different scatter distribution in the phantom. Indeed, the ratio between the average doses absorbed in the whole volume in the evaluation mesh (71% of the phantom volume) in detector view and in extended view, respectively, is 1.997 as derived from the MC simulation. We recall that the reduction in radiation dose depends quantitatively on the experimental conditions chosen, and a 50% dose reduction should not be considered as the value to be expected by using the proposed technique in a practical scan. Indeed, since, in reality, more than 50% view is required in offset scan to ensure good coverage around the isocenter, a dose reduction less than the “ideal” case of 50% could be anticipated. For example, in order to produce reconstructed slices as in Fig. 18, for phantom 2, the detector FOV in projections covered 55% of the object FOV. This factor was the minimum allowed by our software for extended view reconstruction. This required overlapping was not considered in the present MC simulation (i.e., we assumed a FOV coverage  $\sim 50\%$ ) and therefore the actual dose for the offset scan may be higher, in dependence of the actual irradiated volume fraction. This would reduce correspondingly the CNRDs for offset scan and its advantage over the full view scan, yet preserving an advantage in image quality in terms of reduced scatter in the projections. From geometrical considerations, we estimate that, in this work, for our 55% object coverage, the dose reduction in extended view is not lower than 45%; hence, we recalculated the values of CNRD with this new dose estimate (last column of Table II). By comparing CNRD values in the case of 50% dose reduction with these new values (last two columns of Table II), it can be seen that no significant reduction in CNRD is produced.

Figure 10 shows a sample projection of phantom 1 acquired with our CT laboratory setup either in detector

view [Fig. 10(a)] or in extended view [Fig. 10(b)] geometry. Projection images indicate how the phantom is fully included within the field of view in detector view and how it is truncated in extended view. Some internal details are visible inside the phantom in the projections, including longitudinal air-filled holes and calcium filled holes. Overlaid on the projections are drawn intensity profiles along the horizontal broken lines indicated. From such measured projections, by enabling the corresponding option in the reconstruction software, we obtained the CT slices shown in Fig. 11(a) for detector view and extended view acquisition modalities, respectively, for phantom 1; CT number histograms for those coronal slices are shown in Fig. 11(c). Sagittal slices for this scan are shown in Fig. 11(b). The presence of a flatter (less cupping) profile at the center of phantom in extended view is shown both from the line profiles indicated in Fig. 11(b) and from the presence of more populated histograms bins between  $-250$  HU and  $0$  HU in Fig. 11(c). By selecting linear ROIs, as indicated in Fig. 11(a), along the diameter (ROI A) and along a chord through the details (ROI B) shown in the coronal slices, we obtained the profiles shown in Figs. 12(a) and 12(b), respectively. In both geometries, a huge cupping artifact is evident, however, with a lower degree in the case of extended view. Indeed, the non-uniformity index is  $NU = 24\%$  for detector view and  $NU = 14\%$  for extended view, evaluated over circular ROIs (6-mm diameter) in a central coronal slice of phantom 1 (Table I): this indicates a reduced cupping by a factor 1.7 when the extended view geometry is adopted. This reduction, however, comes with an increase of the image noise by a factor  $\sim 2$  (from 32 to 62 HU, Table I).

The profiles shown in Fig. 12(b) indicate qualitatively that all details down to  $\phi = 0.5$  mm are visible. For a quantitative

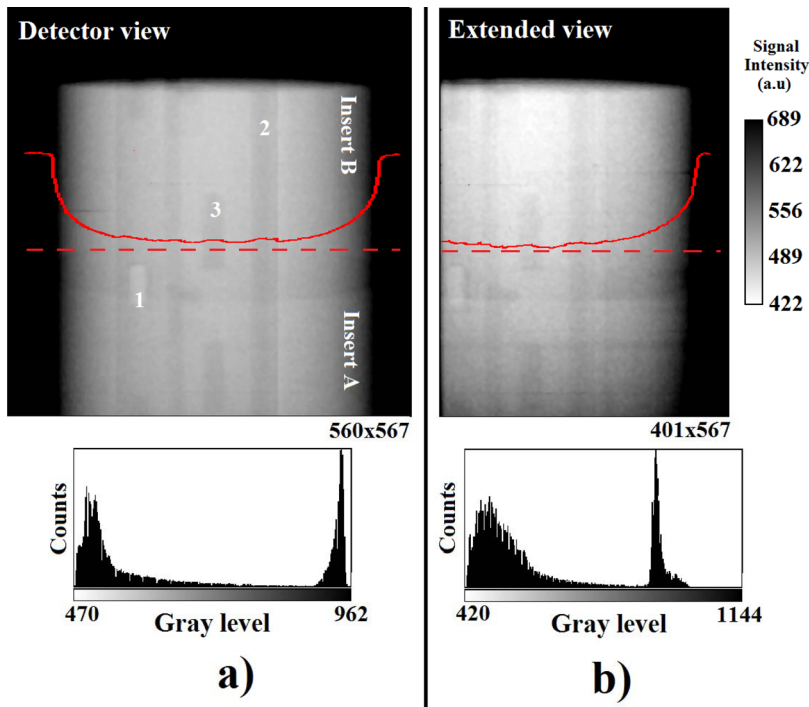


FIG. 10. Measured sample projections of phantom 1 obtained in (a) detector view and b) extended view geometry. Also shown is the gray scale histogram of each projection ( $560 \times 567$  pixels and  $401 \times 567$  pixel, respectively) and the (overlaid) horizontal profile along the dashed lines. Internal details (indicated as 1 =  $\text{CaCO}_3$  filled hole; 2, 3 = air-filled holes) are indicated on the projection. The images have been displayed in an inverted gray scale.

evaluation, we calculated the image quality parameters (contrast  $\Delta\text{HU}$ , CNR, CNRD) for the details contained in Fig. 11(a) (data reported in Table II) as well as global image quality parameters (NU, Noise, rms error, reported in Table I) experimentally determined for phantom 1 on a coronal slice containing no details. Table II shows that, for phantom 1, the detail contrast is between 123 and 1141 HU, that the CNR ranges from 2.4 to 26, and that the CNR for extended view is lower than for detector view in most cases, by a factor  $\sim\sqrt{2}$ , as expected in the case of a dose reduction factor  $\sim 0.5$ . In the same cases, on the other hand, after normalizing the CNR by the simulated radiation dose, the CNRD for extended view is approximately equal to the corresponding value evaluated in detector view (Table II, last column). When the CNR in extended view assumes values equal to or slightly higher than for detector view (nylon 2 mm, air 4 mm, and  $\text{CaCO}_3$  4 mm hole diameter, Table II), also the CNRD, as expected, takes higher values, correspondingly. As regard the image contrast in Table II for phantom 1, for all detail types and sizes  $\Delta\text{HU}$  is systematically higher with the extended view geometry than with the detector view. This is considered a consequence of the decrease of cupping artifact in extended view due to the lower extent of scatter (Fig. 12), which improves the image contrast. We also note that the 0.5-mm air-filled hole is barely detected in the line profiles [Fig. 12(b)], since its size approaches the limiting spatial resolution of this scan. However, in extended view, all the details down to the 0.5-mm size egg-shell fragments can be detected [Fig. 11(d)]: indeed, the values of contrast  $\Delta\text{HU}$  and CNR of  $\text{CaCO}_3$  details 1-mm in size (Table II, insert B) are similar to those for 2-mm-size air-filled details (Table II, insert A).

We point out that, as regards the difference between CNRDs of air in insert A (2-mm details) and in insert B (4-mm details), a partial volume effect could be present, so that for the larger size (4 mm) a better sampling occurs and a

difference in CNRD between extended and detector view comes out (from 9.5 to 5.7). As regards the 2-mm details nylon + air (insert B) and air (insert A), we consider that the hole containing the nylon wires is located more centrally in the phantom than the air-filled hole (see Fig. 3, bottom left). Hence, the scatter reduction operated by the extended view is more effective in increasing the CNRD (from 3.2 to 5.9).

A resolution test is presented in Fig. 12(c) in order to show any difference in spatial resolution between detector and extended view geometries, showing the numerical derivative of the line profiles across the details edges present in Fig. 12(a). In this test, we considered the edges of high contrast details (a 5-mm air-filled hole and the right-hand side edge of the PMMA phantom 1) as providing the edge spread function of the imaging system (in PMMA) in the given experimental conditions, and we searched for a possible difference between the line spread functions in the two geometries, as given by the full width at half maximum (FWHM) of the derivative of those edge spread functions. The Gaussian-fitted FWHM values shown in Fig. 12(c) (0.60 vs 0.64 mm; 0.79 vs 0.85 mm; 0.72 vs 0.65 mm for extended view and detector view, respectively) indicate that there is essentially no loss in spatial resolution between the two imaging techniques.

### III.B. Phantom 2

In a way similar to the analysis done for phantom 1, simulations and acquisitions were performed for the hemiellipsoidal phantom 2 with 140-mm diameter. MC simulations of phantom 2 produced horizontal line profiles along the projections shown in Fig. 13. As in the case of the 70-mm cylindrical phantom, also for this larger phantom, the extended view geometry allows to better approximate the distribution of primary photons inside the phantom, as a result of reduced volume scatter.

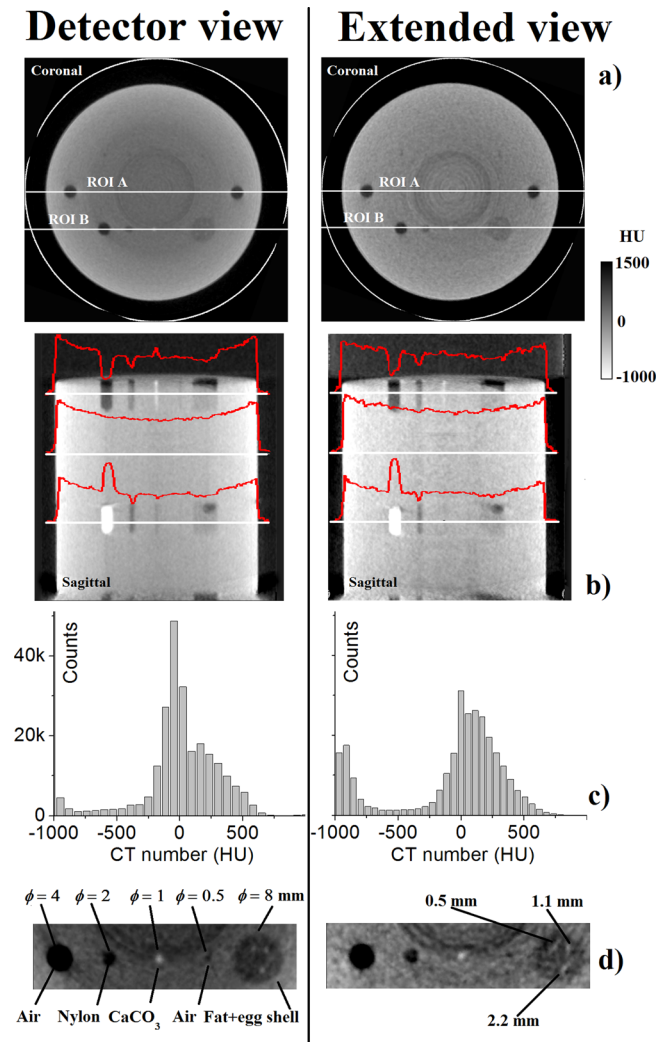


FIG. 11. Reconstructed CT slices of phantom 1 [at 80 kVp] in the detector view (left column) and in the extended view geometry (right column) for (a) a coronal slice and (b) a sagittal slice. On the coronal images are indicated by white lines the two linear ROIs used for profile evaluation, whereas on the sagittal slice are overlaid three line profiles determined over the horizontal white lines shown, drawn across internal details in insert B (upper line), across internal details in insert A (lower line), and across a homogeneous region (central line). (c) Histogram of the CT number values inside the coronal slices. (d) Magnified view of the zone in the phantom around ROI B, showing complete visibility of all details down to the size of 0.5 mm, including the three egg shell fragments (2.2-, 1.1-, and 0.5-mm size) immersed in animal fat.

Images of SPR and scatter distributions and corresponding horizontal profiles in both geometries are reported in Figs. 14 and 15, respectively. The horizontal profiles were evaluated over the rectangular ROIs indicated in Fig. 14. The scatter pattern [Fig. 15(a)] is more intense with detector view and shows a symmetric shape, at variance with extended view in which a large tail extends toward the unirradiated side of the object. The SPR [Fig. 15(b)] is about 0.40 at the center of the phantom for extended view and about 0.75 for detector view, meaning a maximum decrease of SPR of 53%.

Figure 16 shows the profiles evaluated along the diameter of reconstructed coronal slice of phantom 2, derived from the simulated projections. Also, in this case (see Fig. 8 for phan-

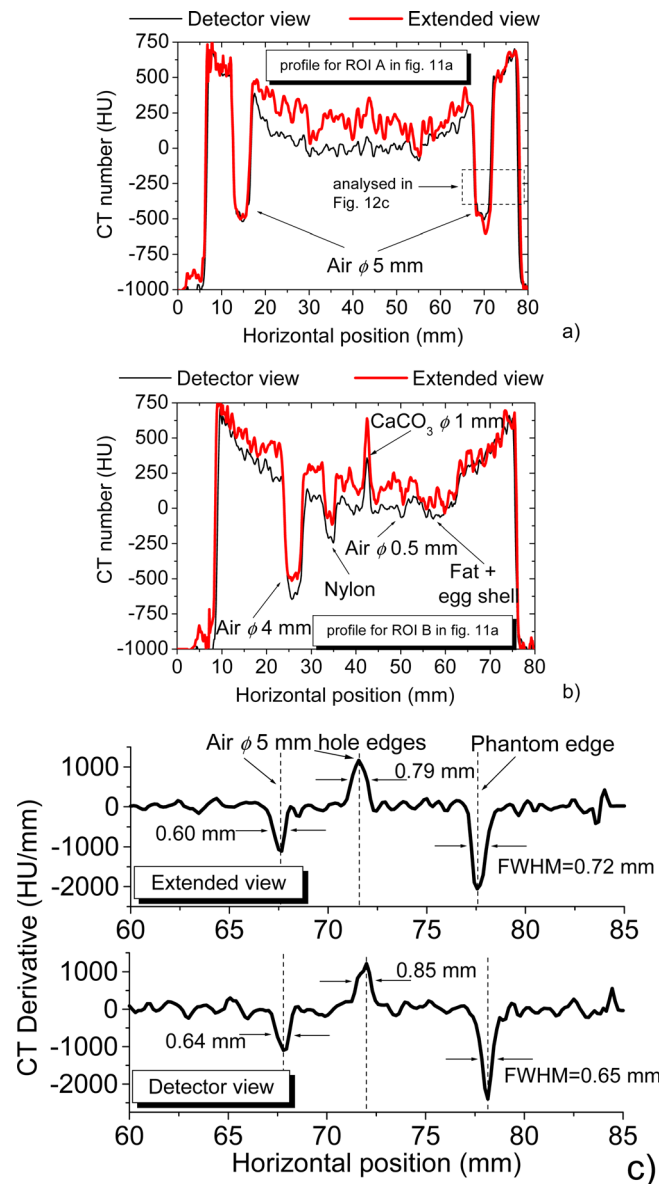


FIG. 12. Horizontal line profiles obtained from (a) ROI A and (b) ROI B indicated in the CT slices of Fig. 11, for detector and for extended views, for phantom 1. Visible details are indicated on the plots. (c) Plots showing the numerical derivative of the line profiles contained in graph (a), relative only to the right-end edge of the PMMA phantom [dashed rectangle in (a)], for detector view (bottom plot) and for extended view (top plot). On the plots are indicated the values of the full width at half maximum (FWHM) evaluated via Gaussian fitting on the edges of the air-filled, 5-mm-size hole, and on the right edge of the phantom.

tom 1, for comparison), the extended view allows to reduce the cupping artifact; however, when comparing this profile with the one obtained by reconstructing only the primary component in the projections, a difference still exists between these two profiles, attributed to only partial correction of the relevant scatter for this larger phantom and to the presence of uncorrected beam hardening [Figs. 15(a) and 16].

As regards the spatial distribution of the absorbed dose, from the simulated dose distributions on a line parallel to the phantom base inside phantom 2 [Fig. 17(a)], one can observe in both geometries the phenomenon of a reduced dose at the center of the phantom (a decrease of about 20%, in rough

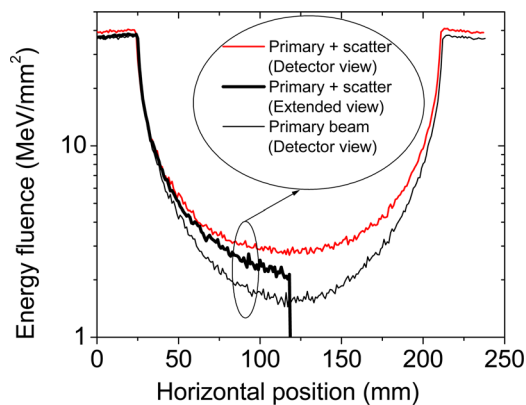


FIG. 13. Horizontal line profiles along simulated total (primary + scatter) and primary projections in detector view geometry, and along the simulated total projection in the extended view geometry, for phantom 2 (a 140-mm diameter hemiellipsoidal phantom).

agreement with our previous findings<sup>39,40</sup>, as well as a lower absolute value of the absorbed dose for the extended view than for the detector view [Fig. 17(b)], as already noted for phantom 1 [see Fig. 9(b)]. The decrease of the dose at the center of the phantom is also evident in Fig. 17(c), which shows a representation of 3D distribution of the absorbed dose simulated in the evaluation mesh inside the phantom volume, for the case of the extended view geometry. A similar plot (but with dose values in the range  $4-6 \times 10^{-8}$  Gy) was obtained in detector view, indicating a reduction of dose by a global factor  $\sim 2$  with respect to the range ( $2-3 \times 10^{-8}$  Gy) found in extended view geometry. Again, we observe that the 50% reduction in dose is connected to the experimental conditions chosen.

CT slices of phantom 2 measured with our scanner are shown in Fig. 18 for coronal and axial views, respectively, in detector view and in extended view. In these scans, the phantom 2 was irradiated with full beam in both geometries but

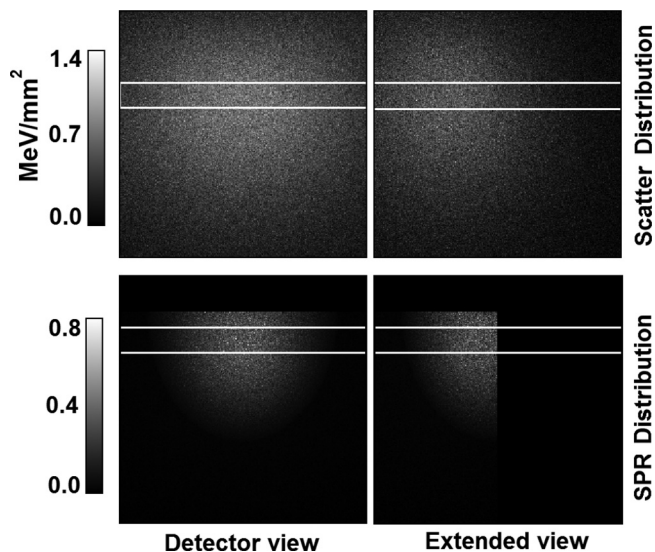


FIG. 14. Images of the simulated scatter and SPR 2D distributions for phantom 2 in detector view (left column) and extended view (right column) geometry.

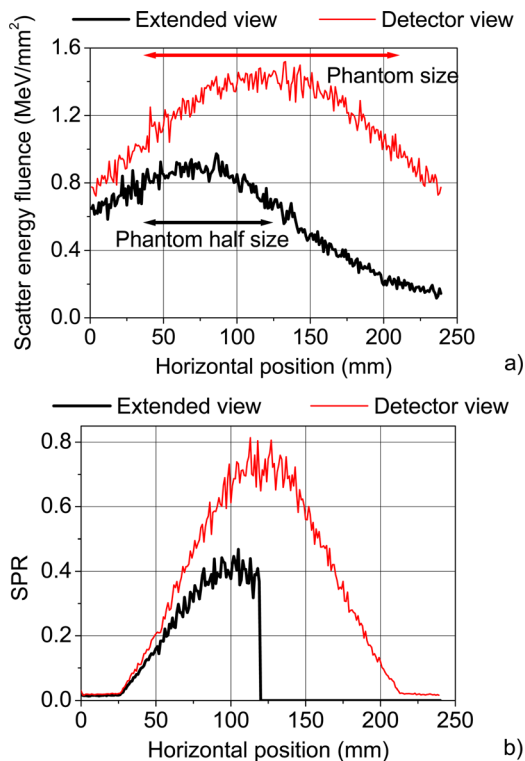


FIG. 15. (a) Scatter and (b) SPR horizontal line profiles (averaged along the columns) obtained from the rectangular ROIs indicated in the simulated projections shown in Fig. 14.

Fig. 18 shows that, in both cases, all the air-filled details are clearly observed down to holes with 1-mm bore size (see phantom description in Fig. 3). In terms of image quality in homogeneous regions in phantom 2, Table I indicates that the cupping artifact is almost the same ( $NU = 18\%$  in extended view and  $19\%$  in detector view), that the image noise is relatively higher (by 5 HU) for extended view (noise = 83 HU) than for detector view (noise = 78 HU), and that the reconstruction rms error is as low as 0.14%. On the other hand, as regards the detail image quality, Table II shows that high contrast details (air-filled holes of 2-mm

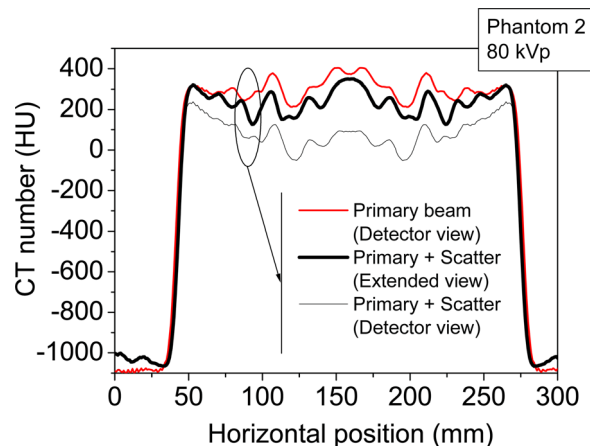


FIG. 16. Profile along the reconstructed coronal slice diameter of simulated 140-mm diameter PMMA hemiellipsoidal phantom in detector and extended view geometry.

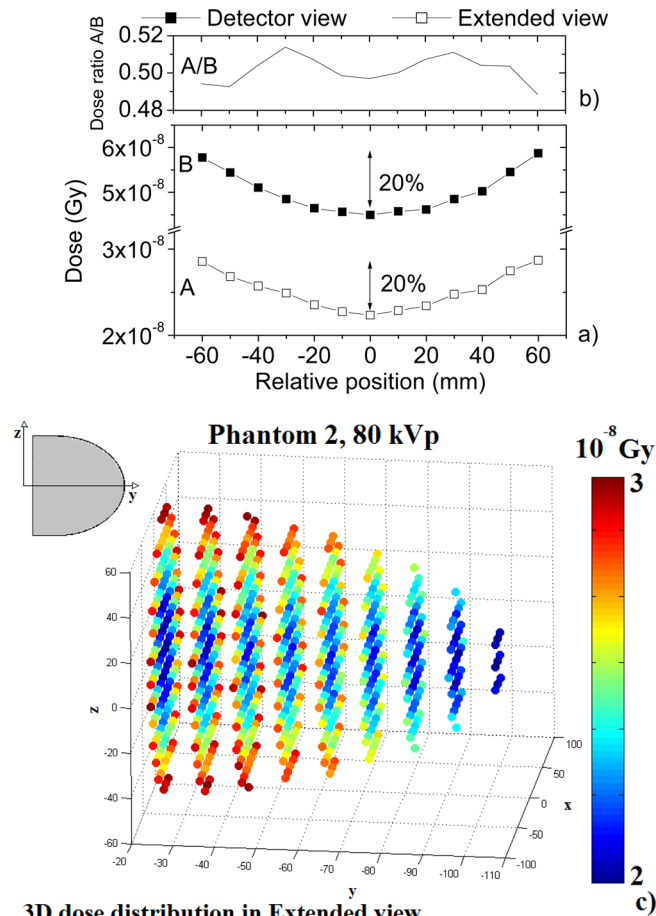


FIG. 17. (a) Horizontal profiles of the absorbed dose along the diameter in detector and extended view geometry, from simulation of phantom 2. (b) Calculated ratio, at each horizontal position, between the dose in extended view and in detector view. (c) 3D plot of the distribution of the absorbed dose in phantom 2 as determined by MC simulation at 80 kVp, in extended view geometry. Each dot represents the position and the value of the dose in  $10 \times 10 \times 10 \text{ mm}^3$  cubic voxel inside an evaluation mesh.

diameter) are seen with close contrast values ( $\Delta\text{HU} = 453 \text{ HU}$  vs  $442 \text{ HU}$ ), less CNR (14 vs 17), and 80% less CNRD ( $6.0$  vs  $7.5$ , in units of  $10^4 \text{ Gy}^{-1/2}$ ) for extended than for detector view, respectively. The line profiles obtained from the rectangular ROIs indicated in the coronal views of Fig. 18 are compared in the plots of Fig. 19. We recall that, in this test with phantom 2, no half beam collimation was used, and hence no scatter or cupping artifact reduction is expected. Figures 18 and 19, and the corresponding data shown in Tables I and II, indicate that, by irradiating the whole phantom 2 and then reconstructing with either geometry, the CT reconstruction made with the extended view produces images with some added noise (5 HU), constant contrast, and 80% reduced CNR and CNRD, with a reconstruction error less than 1%.

IV. DISCUSSION

Simulated reconstructed coronal slices of phantom 1 (a PMMA cylinder with 70-mm diameter), for both the detector view and extended view geometries (Fig. 8 and Table I), illustrate that the latter reconstructions with 50%

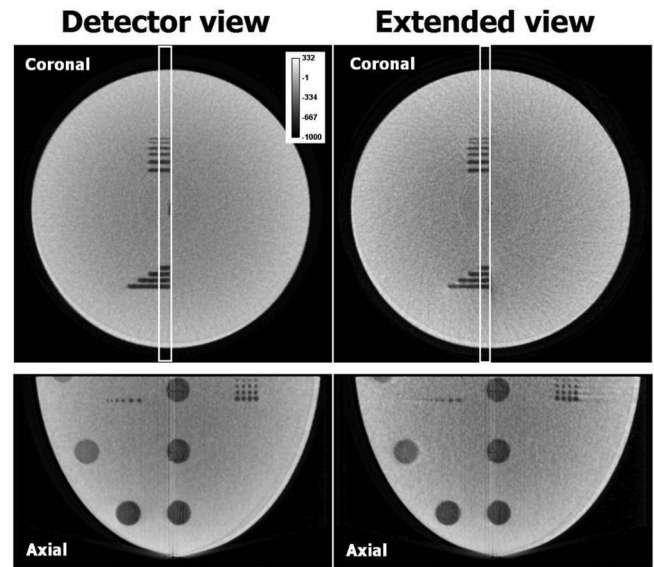


FIG. 18. Reconstructed axial and coronal slices of phantom 2 in detector view (left column) and extended view (right column) geometry, respectively.

half beam irradiation appear less influenced by the cupping artifact (largely contributed by scatter) but noisier by a factor as large as  $\sqrt{2}$  as expected. In the central regions inside this 70-mm large PMMA cylindrical phantom, the extended view geometry shows a reduced cupping (i.e., line profile closer to the simulated primary beam) attributed to a minor influence of scatter [Fig. 7(a)] and to a lower SPR [Fig. 7(b)]. No noticeable distortions due to data truncation are observed using either geometries for the homogeneous simulated phantom 1, as indicated by an rms reconstruction error of just 0.72%. When scanning [at 80 kVp] a real 70-mm-diameter phantom containing contrast details, the extended view geometry produces a similar or larger CNRD with respect to detector view irradiation (phantom 1, Table II), as a result of a lower CNR (by a factor  $\sim 1/\sqrt{2}$ ) and of a lower absorbed dose (by a factor  $\sim 2$ ). In both cases, the contrast details are visible in the CT scan down to 0.5-mm details with a noticeable reduction in the cupping artifact (Figs. 11 and 12). Overall, these findings indicate the correctness of the reconstruction with the half beam

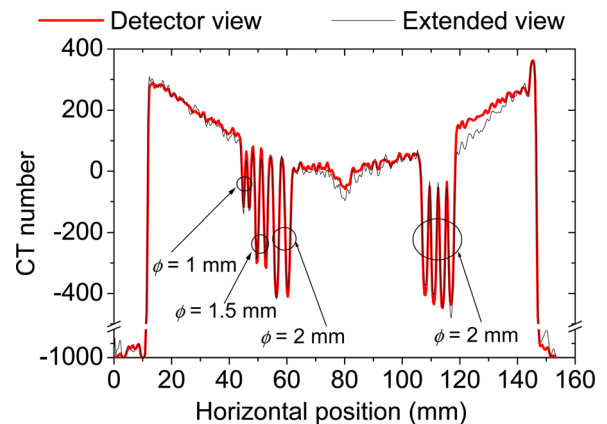


FIG. 19. Line profiles obtained from the ROIs indicated in Fig. 18. All the air-filled holes are visible.

geometry. Moreover, the observed equal or higher values of CNRD give indication of the potential for some reduction in the absorbed dose, while preserving at the same time the image quality (CNR), with respect to the detector view irradiation geometry. The experimenter could then operate the tradeoff between image quality and radiation dose by resorting also to this irradiation geometry; this would be of particular relevance in dose-limited radiological tasks as in breast CT, where the MGD should be limited to values not higher than for two-view mammography and where management of the high SPR problem due to cone-beam geometry is an issue [e.g., average SPR  $\sim 0.3$  for the average uncompressed breast at 80 kVp].

Similarly, for the more realistic phantom 2 scanned with our CT setup, asymmetric datasets provide axial and coronal reconstructions with no truncation artifacts (Fig. 18) and almost identical line profiles than with symmetric datasets (Fig. 19): in this test, no beam collimator was used but an extended view CT reconstruction was performed. The reduction of the cupping artifact seen in Fig. 12 for the 70-mm thick phantom is not visible in the case of the 140-mm thick phantom 2 (Fig. 19): in fact, in this last case the phantom was fully irradiated both in detector view and extended view, thus proving, indirectly, the origin of the expected scatter reduction and cupping reduction when a beam collimator is used to irradiate just one half of the object.

This work gives indication that a possible improvement in image quality, at equal dose, with the proposed extended view geometry could be related to a reduction in scatter by a maximum factor  $\sim 50\%$  due to a corresponding reduction in the irradiated volume. At equal dose, any higher CNR values for extended view than for detector view could be attributed to less noise due to a scatter reduction. Alternatively, the reduced scatter budget could produce some reduction in the dose budget, at equal CNR. In assessing the tradeoff between image quality and dose, one could assume (e.g., Ref. 41) that at a dose level  $D$ , one has  $\text{CNR}^2 \propto D/(1 + \text{SPR})$  and that the ratio of  $\text{CNR}^2$  values in either procedure (subscripts E and D for extended and detector view, respectively) is  $\text{CNR}_E^2/\text{CNR}_D^2 \sim (D_E/D_D)(1 + \text{SPR}_D)/(1 + \text{SPR}_E)$ . This quantity can represent a figure of merit for improvement assessment at a fixed dose or for assessment of the dose reduction obtainable by keeping  $\text{CNR}^2$  the same. This ratio increases in dependence of the amount of scatter reduction as indicated by the SPR metric. Hence, for a half view irradiation with respect to a full view irradiation, knowledge of the SPR in a CBBCT scan allows to estimate this figure of merit, once the expected reduction in scatter is taken into account. In order to obtain an estimate of the practical amount of dose reduction in CBBCT, we consider that at 80 kVp, the SPR at the central axis of cylindrical breast phantoms (composition equivalent to 50% adipose, 50% glandular, or 50/50) is  $\text{SPR} \sim 0.46$  for a 14-cm diameter breast phantom (assumed as the average breast diameter at chest wall).<sup>19</sup> The axial SPR is the maximum value along the cylindrical phantom diameter. From the Gaussian-like shapes of SPR profiles along a diameter as reported in Ref. 19 (given their scan geometry) and confirmed by other studies<sup>20,21</sup> [e.g., see Figs. 7(b)

and 15(b)], one can also estimate that the corresponding average SPR over a diameter is  $\sim 0.28$  for a 14-cm phantom diameter, at 80 kVp. Then, from the results of the present study, one can estimate that the SPR can be reduced by  $\sim 50\%$  [from  $\text{SPR}_D \sim 0.46$  to  $\text{SPR}_E \sim 0.23$  at the central axis of a 14-cm diameter 50/50 breast phantom and, from  $\text{SPR}_D \sim 0.28$  to  $\text{SPR}_E \sim 0.14$  in terms of average SPR, at 80 kVp] by adopting the offset geometry, at any given dose value. As a consequence, from the above considerations, the improvement in  $\text{CNR}^2$  can also be estimated as  $\text{CNR}_E^2/\text{CNR}_D^2 \sim (1 + \text{SPR}_D)/(1 + \text{SPR}_E) \sim (1.46/1.23) \sim 1.19$  (i.e.,  $\text{CNR}_E/\text{CNR}_D \sim 1.09$ ) at equal dose between the two geometries ( $D_E = D_D$ ). On the other hand, by keeping the same  $\text{CNR}^2$  in the detector and extended views ( $\text{CNR}_E^2 = \text{CNR}_D^2$ ), then  $(D_D/D_E) \sim 1.19$  and a potential maximum dose reduction by the same factor  $\sim 19\%$  could be obtained with the offset geometry. In terms of average (instead of maximum) SPR, the dose reduction factor estimated for equal  $\text{CNR}^2$  in the two geometries is  $\sim (1.28/1.14) \sim 12\%$  potential average dose reduction at 80 kVp for a 50/50 breast of 14 cm diameter. This estimate quantifies the average dose reduction theoretically possible in CBBCT for the average 50/50 uncompressed breast as  $\sim 12\%$  in case of minimum image overlapping in extended view. Smaller (larger) breasts would provide a correspondingly lower (higher) dose reduction factor at constant  $\text{CNR}^2$ , respectively, in dependence of the lower (higher) SPR. On the other hand, an overlapping of 5%–10% (i.e., 55%–60% fraction of irradiated volume during a scan in extended view) with a practical setting could decrease such a merit.

From this work, we can state that some reduction in the MGD is feasible in CBBCT by adopting the technique of the displaced detector, thanks to the reduction of the SPR given by the half-irradiation. This advantage is not coupled to a reduction in spatial resolution [at least in the limits of the analysis shown in Fig. 12(c)] and essentially preserves the contrast-to-noise ratio per unit dose.

## V. CONCLUSIONS

We showed the application of a detector displacement technique in cone-beam (breast) computed tomography with a flat panel detector and a beam collimator covering half of the object, using both MC simulations and CT scans of acrylic phantoms. Reconstructed images from our laboratory scanner with the asymmetric detector technique of a 70-mm diameter cylinder and of a realistic 140-mm diameter breast phantom show good agreement with CT images obtained in symmetric conditions. We provided indication that an offset cone-beam geometry allows a wider range of object sizes to be imaged without truncation artifacts or other distortions due to the offset geometry, while producing determination of attenuation coefficients less affected by cupping artifacts and with no loss in spatial resolution. The FOV of our compact system can be nearly doubled with the offset cone beam geometry. There is indication of a decrease in CNR associated with the extended view technique, related to an increase of the noise. At the same time, the proposed method allows to

expose only (about) one-half of the object volume during a scan, offering the possibility of improving the CNR at given imaging dose or reducing somewhat the dose while keeping the CNR the same, with respect to the conventional acquisition method, in relation to the reduction of the SPR. It is estimated that a potential dose reduction  $\sim 12\%$  at 80 kVp at equal CNR could be achieved by irradiating exactly half volume of a 14-cm diameter standard breast of 50% glandular fraction, assuming a reduction of axial SPR from  $\sim 0.46$  to  $\sim 0.23$ . This dose reduction theoretically achievable for the average breast is expected to reduce in practical settings due to the necessity of irradiating a volume fraction slightly higher than 50%. In a contrast detail analysis, the dose advantage produces CNRD values, which are comparable or higher for extended than for detector view. These advantages would be obtained also in the case of a large-area detector used in extended view geometry. Finally, the use of a small flat panel detector allows also to increase the read-out speed and to reduce the overall CBBCT scanner cost.

- <sup>a)</sup> Author to whom correspondence should be addressed. Electronic mail: mettievier@na.infn.it; Telephone: +39-081-676137; Fax: +39-081-676346.
- <sup>1</sup>L. A. Feldkamp, L. C. Davis, and J. W. Kress, "Practical cone-beam algorithm," *J. Opt. Soc. Am. A* **6**, 612–619 (1984).
  - <sup>2</sup>P. S. Cho, A. D. Rudd, and R. H. Johnson, "Cone-beam CT from width-truncated projections," *Comput. Med. Imaging Graph.* **20**, 49–57 (1996).
  - <sup>3</sup>G. Wang, "X-ray micro-CT with a displaced detector array," *Med. Phys.* **29**, 1634–1636 (2002).
  - <sup>4</sup>V. Liu, N. R. Lariviere, and G. Wang, "X-ray micro-CT with a displaced detector array: Application to helical cone-beam reconstruction," *Med. Phys.* **30**, 2758–2761 (2003).
  - <sup>5</sup>A. A. Zamyatin, K. Taguchi, and M. D. Silver, "Helical cone beam CT with an asymmetrical detector," *Med. Phys.* **32**, 3117–3127 (2005).
  - <sup>6</sup>J. M. Boone *et al.*, "Dedicated breast CT: radiation dose and image quality evaluation," *Radiology* **221**, 657–667 (2001).
  - <sup>7</sup>K. K. Lindfors *et al.*, "Dedicated breast CT: Initial clinical experience," *Radiology* **46**, 725–733 (2008).
  - <sup>8</sup>A. O'Connell *et al.*, "Cone-beam CT for breast imaging: Radiation dose, breast coverage, and image quality," *Am. J. Roentgenol.* **195**, 496–509 (2010).
  - <sup>9</sup>B. Chen and R. Ning, "Cone-beam volume CT breast imaging: Feasibility study," *Med. Phys.* **29**, 755–770 (2002).
  - <sup>10</sup>S. J. Glick, "Breast CT," *Annu. Rev. Biomed. Eng.* **9**, 501–526 (2007).
  - <sup>11</sup>M. P. Tornai *et al.*, "Design and development of a fully 3D dedicated x-ray computer mammatomography system," *Proc. SPIE* **5745**, 189–197 (2005).
  - <sup>12</sup>W. T. Yang *et al.*, "Dedicated cone-beam breast CT: Feasibility study with surgical mastectomy specimen," *Am. J. Roentgenol.* **189**, 1312–1315 (2007).
  - <sup>13</sup>W. A. Kalender, "Concepts for high-resolution CT of the breast," In: *Digital Mammography*, edited by J. Martí, A. Oliver, J. Freixenet, R. Martí (Springer-Verlag, Berlin, Heidelberg, 2010), pp. 421–427.
  - <sup>14</sup>P. Russo, A. Lauria, G. Mettievier, and M. C. Montesi, "X-ray cone-beam breast computed tomography: Phantom Studies," *IEEE Trans. Nucl. Sci.* **57**, 160–172 (2010).
  - <sup>15</sup>G. Mettievier *et al.*, "Dedicated scanner for laboratory investigations on cone-beam CT/SPECT imaging of the breast," *Nucl. Instrum. Methods A* **629**, 350–356 (2011).
  - <sup>16</sup>R. van Engen *et al.*, "Addendum on digital mammography," European Guidelines for Quality Assurance in Mammography Screening, Ch. 3, 1.0 ed. (European Reference Organization for Quality Assured Breast Screening and Diagnostic Services, EUREF, Nijmegen, The Netherlands, 2003).
  - <sup>17</sup>D. R. Dance, "Monte Carlo calculation of conversion factors for the estimation of mean glandular breast dose," *Phys. Med. Biol.* **35**, 1211–1219 (1980).

- <sup>18</sup>J. M. Boone, N. Shah, and T. R. Nelson, "A comprehensive analysis of DgN(CT) coefficients for pendant-geometry cone-beam breast computed tomography," *Med. Phys.* **31**, 226–235 (2004).
- <sup>19</sup>A. L. C. Kwan, J. M. Boone, and N. Shah, "Evaluation of x-ray scatter properties in a dedicated cone-beam breast CT scanner," *Med. Phys.* **32**, 2967–2975 (2005).
- <sup>20</sup>Y. Chen *et al.*, "Characterization of scatter in cone-beam CT breast imaging: Comparison of experimental measurements and Monte Carlo simulation," *Med. Phys.* **36**, 857–869 (2009).
- <sup>21</sup>G. Mettievier, P. Russo, N. Lanconelli, and S. Lo Meo, "Evaluation of scattering in Cone-Beam breast computed tomography: A Monte Carlo and experimental phantom study," *IEEE Trans. Nucl. Sci.* **57**, 2510–2517 (2010).
- <sup>22</sup>J. M. Boone and J. A. Seibert, "Monte-Carlo simulation of the scattered radiation distribution in diagnostic-radiology," *Med. Phys.* **15**, 713–720 (1988).
- <sup>23</sup>D. A. Jaffray *et al.*, "X-ray scatter in megavoltage transmission radiography-physical characteristics and influence on image quality," *Med. Phys.* **21**, 45–60 (1994).
- <sup>24</sup>G. Jarry *et al.*, "Monte Carlo investigation of scatter contribution to kilovoltage cone-beam computed tomography images," *Med. Phys.* **32**, 2092 (2005).
- <sup>25</sup>W. Zbijewski, A. P. Colijn, and F. J. Beekman, "Monte Carlo based scatter correction for cone-beam micro-CT," *Proc. 7th Int. Conf. on Fully 3D Reconstruction in Radiology and Nuclear Medicine* (Saint Malo, France, 2003).
- <sup>26</sup>G. Jarry *et al.*, "Characterization of scattered radiation in kV CBCT images using Monte Carlo simulations," *Med. Phys.* **33**, 4320–4329 (2006).
- <sup>27</sup>E. P. Ruhmschopf and K. Klingensbeck, "A general framework and review of scatter correction methods in x-ray cone-beam computerized tomography. Part 1: Scatter compensation approaches," *Med. Phys.* **38**, 4296–4303 (2011).
- <sup>28</sup>G. Mettievier and P. Russo, "Measurement of the MTF of a cone-beam breast computed tomography laboratory scanner," *IEEE Trans. Nucl. Sci.* **58**, 703–713 (2011).
- <sup>29</sup>K. Yang, A. L. C. Kwan, and J. M. Boone, "Computer modeling of the spatial resolution properties of a dedicated breast CT system," *Med. Phys.* **34**, 2059–2069 (2007).
- <sup>30</sup>S.-Y. Huang *et al.*, "The characterization of breast anatomical metrics using dedicated breast CT," *Med. Phys.* **38**, 2180–2191 (2011).
- <sup>31</sup>S. Agostinelli *et al.*, "GEANT4—A simulation toolkit," *Nucl. Instrum. Methods A* **506**, 250–303 (2003).
- <sup>32</sup>J. Allison *et al.*, "GEANT4 developments and applications," *IEEE Trans. Nucl. Sci.* **53**, 270–278 (2006).
- <sup>33</sup>K. Amako *et al.*, "Comparison of GEANT4 electromagnetic physics models against the NIST reference data," *IEEE Trans. Nucl. Sci.* **52**, 910–918 (2005).
- <sup>34</sup>J. M. Boone, and J. A. Seibert, "An accurate method for computer-generating tungsten anode x-ray spectra from 30 to 140 kV," *Med. Phys.* **24**, 1661–1670 (1997).
- <sup>35</sup>J. M. Boone *et al.*, "Technique factors and their relationship to radiation dose in pendant geometry breast CT," *Med. Phys.* **32**, 3767–3776 (2005).
- <sup>36</sup>COBRA Software Package Version 7.1, User Manual (2011).
- <sup>37</sup>H. Bruning and S. Gouzev, Exxim Computing Corporation, Pleasanton, CA (private communication).
- <sup>38</sup>D. L. Parker, "Optimal short scan convolution reconstruction for fanbeam CT," *Med. Phys.* **9**, 254–257 (1982).
- <sup>39</sup>P. Russo, T. Coppola, and G. Mettievier, "Distribution of absorbed dose in cone-beam breast computed tomography: A phantom study with radiochromic films," *IEEE Trans. Nucl. Sci.* **57**, 2220–2229 (2010).
- <sup>40</sup>P. Russo *et al.*, "Distribution of absorbed dose in cone-beam breast computed tomography: An experimental phantom study," *IEEE Trans. Nucl. Sci.* **57**, 366–374 (2010).
- <sup>41</sup>K. J. Engel, C. Herrmann, and G. Zeitler, "X-ray scattering in single- and dual-source CT," *Med. Phys.* **35**, 318–332 (2008).